Tailoring the Magnetism of Co Atoms on Graphene through Substrate Hybridization

F. Donati,[1] L. Gragnaniello,[1,*] A. Cavallin,[1,†] F. D. Natterer,[1,‡] Q. Dubout,[1] M. Pivetta,[1] F. Patthey,[1] J. Dreiser,[1,2] C. Piamonteze,[2] S. Rusponi,[1] and H. Brune[1]

[1]*Institute of Condensed Matter Physics (ICMP), École Polytechnique Fédérale de Lausanne (EPFL), Station 3, CH-1015 Lausanne, Switzerland*

[2]*Swiss Light Source (SLS), Paul Scherrer Institut (PSI), CH-5232 Villigen PSI, Switzerland*

(Received 9 April 2014; published 20 October 2014)

We determine the magnetic properties of individual Co atoms adsorbed on graphene (G) with x-ray absorption spectroscopy and magnetic circular dichroism. The magnetic ground state of Co adatoms strongly depends on the choice of the metal substrate on which graphene is grown. Cobalt atoms on G/Ru(0001) feature exceptionally large orbital and spin moments, as well as an out-of-plane easy axis with large magnetic anisotropy. Conversely, the magnetic moments are strongly reduced for Co/G/Ir(111), and the magnetization is of the easy-plane type. We demonstrate how the Co magnetic properties, which ultimately depend on the degree of hybridization between the Co $3d$ orbitals and graphene π bands, can be tailored through the strength of the graphene-substrate coupling.

DOI: 10.1103/PhysRevLett.113.177201 PACS numbers: 75.30.Gw, 61.48.Gh, 75.10.Dg, 78.70.Dm

Graphene (G) recently emerged as one of the most promising materials for spintronics [1]. It was proposed as a perfect spin filter between two ferromagnetic electrodes [2,3], isolated adsorbed magnetic impurities were employed to tailor its electronic [4,5] and spin transport properties [6], and it was used as a capping layer to increase the magnetic anisotropy of ultra thin films [7,8]. In addition, giant magnetic anisotropies were predicted for $3d$ metal atoms and dimers on graphene [9,10] or on graphene C vacancies [11], suggesting long spin relaxation times with the potential for quantum information processing in single adatoms.

The magnetic properties of transition metal atoms on graphene strongly depend on the on-site Coulomb interaction [12–14], whose screening is determined by the graphene local density of states around the Fermi level, E_F [15]. The latter can be adjusted by the graphene-substrate hybridization [16] creating the possibility of tailoring the magnetism of transition metal atoms adsorbed onto graphene. Here, we demonstrate this concept by controlling the magnetic properties of Co adatoms up to the point of turning the easy magnetization direction from in plane to out of plane.

We use x-ray absorption spectroscopy (XAS) and x-ray magnetic circular dichroism (XMCD) to reveal the magnetism of ensembles of individual Co atoms adsorbed on graphene grown on Ru(0001) and Ir(111). While most of the G layer hybridizes strongly with Ru [17], it interacts essentially only by van der Waals forces with Ir [18], as reflected in the very different binding distances of the respective moiré minima of 2.1 versus 3.4 Å [19]. Both metal substrates allow the growth of defect-free monolayer graphene with a filling factor of 1 [20,21], thereby enabling Co adatom ensemble measurements. On G/Ru(0001), we find large Co spin and orbital moments with out-of-plane easy axis and very high magnetic anisotropy. In contrast, Co atoms on G/Ir(111) show much lower spin and negligible orbital moments, and they have an out-of-plane hard axis. These findings exemplify the decisive role played by graphene-substrate hybridization on the magnetic properties of single atoms.

We performed XAS and XMCD measurements at the X-Treme beam line of the Swiss Light Source [22]. XAS spectra were recorded with circularly polarized light in the total electron yield (TEY) mode at the Co $L_{2,3}$ absorption edges at $T = 2.5$ K and in magnetic fields up to $B = 6.8$ T parallel to the x-ray beam. The spectra were normalized to the intensity of the x-ray beam measured on a metallic grid placed upstream of the sample, and in addition to their preedge values at 768.5 eV in order to account for the different TEY efficiencies at normal (0°) and grazing (70°) incidence. The XMCD signal is the difference between the XAS recorded for parallel μ_+ and antiparallel μ_- alignment of the photon helicity with respect to the direction of the applied field. Each pair of μ_+ and μ_- spectra was acquired on a different spot of the sample to prevent beam-induced modifications of the XAS signal [23]. Single crystals of Ru(0001) and Ir(111) were prepared *in situ* by means of Ar^+ sputtering and annealing (1400 K) cycles in the preparation chamber of the X-Treme end station. A single layer of graphene was grown by chemical vapor deposition (100 Langmuir C_2H_4 at 1400 K) and the quality checked with an Omicron VT scanning tunneling microscope (STM) connected to the preparation chamber. Cobalt was deposited from high purity rods (99.995%) using a commercial *e*-beam evaporator onto the sample held at about 3.5 K in the measurement position at a background pressure of $p_{\mathrm{tot}} \leq 5 \times 10^{-11}$ mbar. The Co coverage (Θ) was calibrated by mapping the covered area with the STM at room

temperature for close to half-monolayer coverage, and this calibration was used in XAS by evaluating the integrated Co $L_{2,3}$ signal for the same sample. One monolayer (ML) is defined as one Co atom per substrate atom. For samples prepared under identical conditions as those measured with XMCD, we determined the adsorption site, the fraction of Co monomers and dimers in the ensemble, and their local electronic properties with a home-built low temperature (4.7 K) STM. Multiplet calculations were performed using the CTM4XAS55 code [24]. The initial model parameters were taken from literature [12,13] and iteratively refined to reproduce our experimental spectra (see the Supplemental Material [25]).

Figure 1(a) shows the XAS spectra of 0.01 ML of Co/G/Ru(0001) for normal and grazing photon incidence. At this low Co coverage, the $L_{2,3}$ edges appear as small peaks on top of the substrate background. A STM image of 0.008 ML of Co on G/Ru(0001) is shown in Fig. 1(b). The (23×23) moiré [42,43] is imaged as four different hills per unit cell [17,44]. Following the statistical analysis outlined in Refs. [45,46] and in the Supplemental Material [25], we find that the majority of the protrusions are single Co adatoms ($93.0 \pm 0.4\%$), the remaining species are dimers. In addition, we verified that hydrogen coadsorption is negligible [46,47]. The XAS signal is also quite different from that of an ensemble of small clusters (see the Supplemental Material [25]). To a very good approximation, therefore, it stems from an ensemble of clean and isolated Co monomers. Moreover, the fine multiplet structure observed in the XAS and XMCD spectra indicates that a large part of the atoms of this ensemble have a very similar electronic structure. Our STM measurements reveal that the majority ($81 \pm 2\%$) of the Co atoms are adsorbed in the moiré valleys that make up 2/3 of the surface structure [48]. These atoms are featureless in scanning tunneling spectroscopy in the range of ± 40 meV around E_F. The remaining $19 \pm 2\%$ of the Co atoms are situated close to the moiré hills and exhibit characteristic Kondo features in their differential conductance [25,49]. Effects of this minority species on the measured XAS signal will be discussed further below.

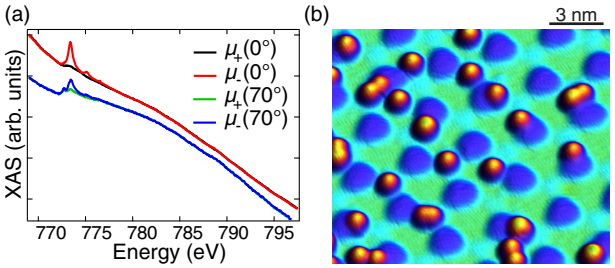

FIG. 1 (color online). (a) Normalized XAS spectra of Co atoms on G/Ru(0001) taken at normal and grazing incidence ($\Theta = 0.01$ ML, $B = 6.8$ T, $T = 2.5$ K). The spectra are offset for clarity. (b) STM image of 0.008 ML Co on G/Ru(0001) (mean cluster size 1.07 ± 0.04 atoms, $V_t = -50$ mV, $I_t = 100$ pA, $T = 4.7$ K).

The magnetic properties and the electronic configuration of the Co adatoms emerge from XAS spectra after subtracting the substrate signal and absorption edge step functions, see Figs. 2(a) and 2(b). A fine multipeak structure is visible for both normal and grazing incidence. In contrast to Co/G/SiC [50] and to Co on bare Ru(0001) (see the Supplemental Material [25]), we find an exceptionally strong dichroism for both incidence geometries, indicating large magnetic moments localized on the Co adatoms. Moreover, the remarkable difference between normal and grazing incidence XMCD reveals a strong uniaxial magnetic anisotropy with an out-of-plane easy axis.

Insight into the electronic structure and the crystal field acting on the Co atoms is obtained from multiplet calculations. As evidenced in Fig. 2(a), the calculated spectra agree very well with the experiment. They reveal a mixed $d^7 + d^8$ configuration with a number of d holes (n_h) of about 2.5. The calculations, further, show that the degeneracy of the d orbitals is lifted by an almost purely uniaxial crystal field, producing an a_1 singlet (d_{z^2}) and two doublets e_1 (d_{xz}, d_{yz}) and e_2 ($d_{x^2-y^2}, d_{xy}$), respectively. The corresponding splitting of d orbitals is shown in Fig. 2(c) and resembles closely the prediction for a Co atom adsorbed on the graphene top site [12]. The a_1 singlet is lowest in energy, pointing towards the formation of an out-of-plane bond responsible for the high perpendicular anisotropy (see the Supplemental Material [25]).

Quantitative values of the orbital (m_L) and effective spin magnetic moment (given by the sum of the spin and dipolar

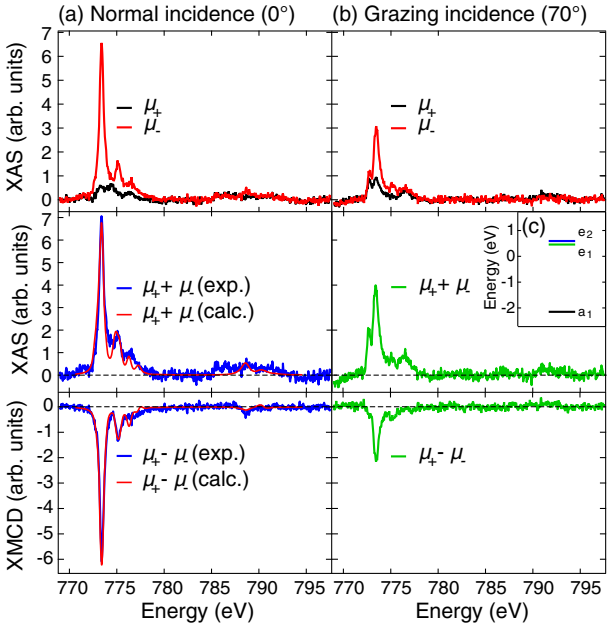

FIG. 2 (color online). (a) and (b) Background subtracted XAS and XMCD of Co/G/Ru(0001), together with normal incidence spectra from the multiplet calculations [$\Theta = 0.01$ ML, $B = 6.8$ T, $T = 2.5$ K, average over 10 (a), respectively, 5 (b) spectra]. (c) Splitting of d orbitals induced by the uniaxial crystal field according to multiplet calculations.

TABLE I. Effective spin and orbital magnetic moments (in μ_B), as well as their sum and ratio, of Co/G/Ru(0001) for normal (0°) and grazing (70°) incidence obtained from experiment (Exp.) using the sum rules with $n_h = 2.5$. For normal incidence, values corrected (Corr.) for the Kondo screened species and results from multiplet calculations (Mult.) are reported for comparison.

	Exp. (0°)	Corr. (0°)	Mult. (0°)	Exp. (70°)
m_{S+D}	2.26 ± 0.22	2.79	2.95	1.25 ± 0.13
m_L	1.71 ± 0.16	2.11	2.15	0.54 ± 0.06
$m_{S+D} + m_L$	3.97 ± 0.27	4.90	5.10	1.79 ± 0.14
m_L/m_{S+D}	0.76 ± 0.14	0.76	0.73	0.43 ± 0.09

terms, m_{S+D}) projected onto the x-ray incidence direction can be obtained from the integrated XAS and XMCD by application of the sum rules [51,52]. As described in Ref. [53], one needs to account for the strong angular variation of the XAS intensity (see the Supplemental Material [25]). For the individual moments, we used $n_h = 2.5$ from the multiplet calculations. The ratio m_L/m_{S+D} is obtained without assumptions on n_h and from XMCD alone, which makes it very robust with respect to background subtraction. The resulting magnetic moments, as well as their ratios, are given in Table I. For comparison, we also show normal incidence values obtained from multiplet calculations. The out-of-plane m_L value is one of the largest so far reported for magnetic adatoms [54–56]. Also, the anisotropy of m_L is exceptionally high, as emphasized by the strong angular variation of the ratio m_L/m_{S+D} [57]. Multiplet calculations show excellent agreement with the value of m_L/m_{S+D} at normal incidence obtained from the sum rules, but overestimate m_{S+D} and m_L by 25%–30%. We attribute this to the fraction of Co atoms whose magnetic moments are Kondo screened, thus, giving little or no dichroic contribution [58]. Assuming full screening of the magnetic moment, we corrected for the Kondo species and obtained the m_{S+D} and m_L values of the majority population, which agrees very well with those deduced from the multiplet calculations, see Table I.

The magnetic anisotropy K per atom has been quantified by fitting the normal and grazing incidence magnetization curves shown in Fig. 3. In the paramagnetic limit, the expectation value of the Co magnetization can be modeled as [55]

$$M = M_{\mathrm{sat}} \frac{\int_0^{2\pi} d\phi \int_0^{\pi} \sin\theta \cos\theta e^{E/k_B T} d\theta}{\int_0^{2\pi} d\phi \int_0^{\pi} \sin\theta e^{E/k_B T} d\theta}, \qquad (1)$$

where M_{sat} is the saturation magnetization, ϕ and θ are the polar and azimuthal angles of the total magnetic moment m with respect to the surface normal, the energy E is the sum of the Zeeman term $mB\cos\theta$ and the magnetic anisotropy term $-K(\sin\theta_0 \sin\theta \cos\phi + \cos\theta_0 \cos\theta)^2$ at a photon incidence angle θ_0. From the fit, we obtain $m = 5.2 \pm 1.0\,\mu_B$ and $K = 8.4 \pm 2.9$ meV. We note that a quantum mechanical model based on an effective spin Hamiltonian yields m and K values that agree within the error bars (see the Supplemental Material [25]).

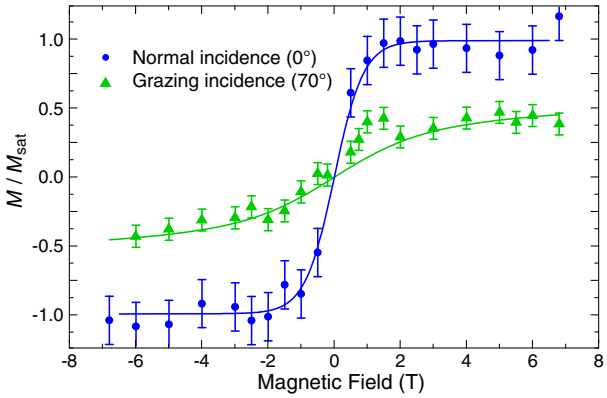

FIG. 3 (color online). Magnetization curve of Co/G/Ru(0001) ($\Theta = 0.01$ ML, $T = 2.5$ K). The points correspond to the maximum of the XMCD obtained from a single pair of μ_+ and μ_- spectra. Since each of them is measured on a different surface spot, we accounted for intensity variations by dividing by the maximum of the background subtracted XAS at the Co L_3 edge. The XMCD maxima are proportional to the total moments of a Co atom, but are less accurate than the full sum rule analysis taking into account integrals over both $L_{2,3}$ edges. Therefore, we scaled the normal and grazing curves such that their ratio at 6.8 T is equal to the ratio of the corresponding total moments from sum rules, see Table I. The solid lines show the fits with Eq. (1).

For $3d$ transition metals with $n_h < 5$, spin and orbital moments have parallel alignment; therefore, the total atomic moment is $m = m_S^d + m_S^s + m_L$, where m_S^d and m_S^s denote the spin moments due to d and s orbitals, respectively. In order to circumvent the XMCD sensitivity issues for s orbitals [59], we use the value of 0.5 μ_B for m_S^s predicted by density functional theory (DFT) calculations [12]. Taking the corrected values of $m_S^d \approx m_{S+D}$ [57] and m_L from Table I, we obtain $5.4 \pm 0.3\,\mu_B$, in excellent agreement with the value obtained from the magnetization curves.

The remarkably large anisotropy K approaches the largest values measured for transition metal adatoms on metal and on graphene [47,55], once more illustrating the great potential of graphene to induce large uniaxial magnetic anisotropy. The observation of an out-of-plane easy axis in Co/G/Ru(0001) as opposed to Co/G/Pt(111) [47], both with high anisotropy, is the first evidence of control of the magnetic properties by substrate hybridization.

To further illustrate this concept, we now turn to our second system Co/G/Ir(111), displaying very different magnetic properties and electronic configuration of the adatoms. Figure 4 shows the absence of a fine multipeak structure in XAS that is indicative of a stronger hybridization between Co and graphene orbitals. The L_3 and L_2 peaks have opposite signs in the XMCD spectrum resulting from a strongly reduced orbital moment compared to the preceding system. The XMCD signal is largest at grazing

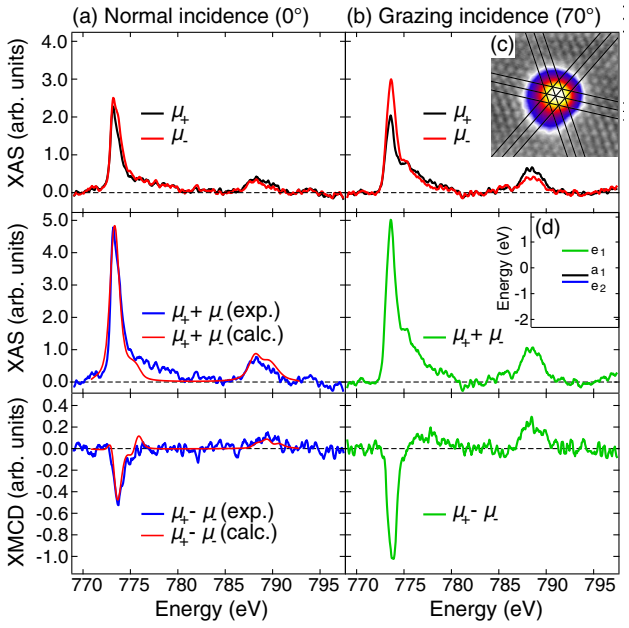

FIG. 4 (color online). (a) and (b) Background subtracted XAS and XMCD of Co/G/Ir(111), together with normal incidence spectra simulated with multiplet calculations ($\Theta = 0.01$ ML, $B = 6.8$ T, $T = 2.5$ K, (a) and (b) average over six spectra). (c) Adsorption site deduced from STM image of a Co atom on G/Ir(111) with atomically resolved graphene. Black lines mark the sixfold graphene hollow sites imaged as protrusions (3.2×3.2 nm^2, $V_t = -50$ mV, $I_t = 200$ pA, $T = 4.7$ K). (d) Splitting of d orbitals induced by the uniaxial crystal field according to multiplet calculations.

incidence, revealing an out-of-plane hard axis. Multiplet calculations show an almost pure d^8 configuration with $n_h \approx 1.85$, i.e., $S \approx 1$ (see the Supplemental Material [25]). As expected for an $S = 1$ system with an out-of-plane hard axis, neither the in-plane nor the out-of-plane magnetization curves (not shown) saturate at $B = 6.8$ T and $T = 2.5$ K [60]. Therefore, the atomic magnetic moments obtained from the sum rules given in Table II represent lower bounds to the real values. The atomically resolved STM image shown in Fig. 4(c) reveals that Co adsorbs on the sixfold graphene hollow site. The level splitting of the d orbitals shown in Fig. 4(d) agrees very well with the one predicted by DFT for this adsorption site [12].

Putting the present results into relation with the magnetic properties found for Co/G/Pt(111) [47], we derive a clear correlation between the number of holes in the Co $3d$ orbitals and the strength of the graphene-substrate interaction which is stronger for $4d$ and weaker for $5d$ metals [61]. The number of holes increases from 1.85 for G/Ir(111) via 2.0 for G/Pt(111) to 2.5 for G/Ru(0001), accompanied, as expected, by increasing spin moments. The orbital moments also follow this trend. Similarly, the preferred magnetization direction depends on graphene-substrate hybridization; it lies in plane for Co on G/Ir(111) and on G/Pt(111) [47], whereas it is out-of-plane for Co on G/Ru(0001).

TABLE II. Effective spin and orbital magnetic moments of Co/G/Ir(111), as well as their sum and ratio, estimated from the sum rules using $n_h = 1.85$.

	Normal (0°)	Grazing (70°)
m_{S+D} (μ_B)	0.45 ± 0.04	0.57 ± 0.04
m_L (μ_B)	0.09 ± 0.02	0.04 ± 0.02
$m_{S+D} + m_L$ (μ_B)	0.54 ± 0.05	0.61 ± 0.05
m_L/m_{S+D}	0.19 ± 0.06	0.07 ± 0.04

These findings can be interpreted in the light of the competing hybridization of the graphene π bands with both the substrate d bands and Co $3d$ orbitals. The degree of hybridization of the first is tailored by choosing a specific metal substrate. For G/Ru(0001), the strong hybridization with the substrate d bands opens a gap of about 2 eV in the graphene π bands just below E_F [62,63]. This gap limits the hybridization between Co and graphene orbitals and preserves a largely unscreened Coulomb interaction. On the other hand, for G/Pt(111) and G/Ir(111), the interaction between the substrate and graphene is weak and leaves the graphene π bands almost unperturbed [64–66], allowing for a stronger hybridization between Co and graphene and an effective screening of the Coulomb interaction.

Finally, we can correlate the values of the orbital magnetic moment and the change of the easy magnetization direction with the occupation and splitting of the $3d$ orbitals obtained from multiplet calculations. For Co/G/Ru(0001), the diagonal e_1 and the planar e_2 orbitals are highest in energy and almost degenerate; therefore, most of the 2.5 holes are shared between these two doublets. In particular, the hole localized in the e_2 orbitals preserves a large orbital magnetic moment and favors a perpendicular anisotropy [67]. This behavior is similar to individual Co atoms on MgO/Ag(100), where a large unscreened Coulomb interaction, due to the wide MgO band gap centered at Fermi level, favors fully unquenched orbital moments and maximum magnetic anisotropy [68]. The orbital splitting found for Co/G/Ir(111) is, instead, quite similar to the one calculated for Co/G/Pt(111) [47]. In this case, the two holes are localized in the uppermost e_1 orbitals. This configuration leads to the quenching of the orbital moment and favors an out-of-plane hard axis.

In conclusion, we have demonstrated how the magnetic properties of Co atoms adsorbed on graphene can be tailored by choosing the appropriate metal substrate. In particular, the complex interplay between the Co $3d$ orbitals and the graphene π bands, modified by the underlying substrate, can generate large magnetic moments and perpendicular magnetic anisotropy in Co atoms, two fundamental requirements for information storage devices and manipulation of single magnetic atoms.

We acknowledge funding from the Swiss National Science Foundation and from the Sino-Swiss Science and Technology Cooperation Project No. IZLCZ2 123892.

*Present address: Fachbereich Physik, Universität Konstanz, D-78457 Konstanz, Germany.
†Present address: Max-Planck-Institut für Mikrostrukturphysik, D-06120 Halle (Saale), Germany.
‡Present address: Center for Nanoscale Science and Technology, NIST, Gaithersburg, MD 20899, USA.

[1] N. Tombros, C. Jozsa, M. Popinciuc, H. T. Jonkman, and B. J. van Wees, Nature (London) **448**, 571 (2007).
[2] V. M. Karpan, G. Giovannetti, P. A. Khomyakov, M. Talanana, A. A. Starikov, M. Zwierzycki, J. van den Brink, G. Brocks, and P. J. Kelly, Phys. Rev. Lett. **99**, 176602 (2007).
[3] O. V. Yazyev and A. Pasquarello, Phys. Rev. B **80**, 035408 (2009).
[4] V. W. Brar, R. Decker, H. M. Solowan, Y. Wang, L. Maserati, K. T. Chan, H. Lee, Ç. O. Girit, A. Zettl, S. G. Louie, M. L. Cohen, and M. F. Crommie, Nat. Phys. **7**, 43 (2011).
[5] Y. Wang, V. W. Brar, A. V. Shytov, Q. Wu, W. Regan, H. Z. Tsai, A. Zettl, L. S. Levitov, and M. F. Crommie, Nat. Phys. **8**, 653 (2012).
[6] K. Pi, W. Han, K. M. McCreary, A. G. Swartz, Y. Li, and R. K. Kawakami, Phys. Rev. Lett. **104**, 187201 (2010).
[7] N. Rougemaille, A. T. N'Diaye, J. Coraux, C. Vo-Van, O. Fruchart, and A. K. Schmid, Appl. Phys. Lett. **101**, 142403 (2012).
[8] R. Decker, J. Brede, N. Atodiresei, V. Caciuc, S. Blügel, and R. Wiesendanger, Phys. Rev. B **87**, 041403 (2013).
[9] R. J. Xiao, D. Fritsch, M. D. Kuz'min, K. Koepernik, H. Eschrig, M. Richter, K. Vietze, and G. Seifert, Phys. Rev. Lett. **103**, 187201 (2009).
[10] M. Sargolzaei and F. Gudarzi, J. Appl. Phys. **110**, 064303 (2011).
[11] H. C. Kandpal, K. Koepernik, and M. Richter, Phys. Rev. B **86**, 235430 (2012).
[12] T. O. Wehling, A. V. Balatsky, M. I. Katsnelson, A. I. Lichtenstein, and A. Rosch, Phys. Rev. B **81**, 115427 (2010).
[13] T. O. Wehling, A. I. Lichtenstein, and M. I. Katsnelson, Phys. Rev. B **84**, 235110 (2011).
[14] A. N. Rudenko, F. J. Keil, M. I. Katsnelson, and A. I. Lichtenstein, Phys. Rev. B **86**, 075422 (2012).
[15] D. Jacob and G. Kotliar, Phys. Rev. B **82**, 085423 (2010).
[16] A. Dahal, R. Addou, H. Coy-Diaz, J. Lallo, and M. Batzill, APL Mat. **1**, 042107 (2013).
[17] M. Iannuzzi, I. Kalichava, H. Ma, S. J. Leake, H. Zhou, G. Li, Y. Zhang, O. Bunk, H. Gao, J. Hutter, P. R. Willmott, and T. Greber, Phys. Rev. B **88**, 125433 (2013).
[18] C. Busse, P. Lazić, R. Djemour, J. Coraux, T. Gerber, N. Atodiresei, V. Caciuc, R. Brako, A. T. NDiaye, S. Blügel, J. Zegenhagen, and T. Michely, Phys. Rev. Lett. **107**, 036101 (2011).
[19] M. Batzill, Surf. Sci. Rep. **67**, 83 (2012).
[20] J. Wintterlin and M. L. Bocquet, Surf. Sci. **603**, 1841 (2009).
[21] F. D. Natterer, S. Rusponi, M. Papagno, C. Carbone, and H. Brune, J. Phys. Condens. Matter **24**, 314203 (2012).
[22] C. Piamonteze, U. Flechsig, S. Rusponi, J. Dreiser, J. Heidler, M. Schmidt, R. Wetter, M. Calvi, T. Schmidt, H. Pruchova, J. Krempasky, C. Quitmann, H. Brune, and F. Nolting, J. Synchrotron Radiat. **19**, 661 (2012).
[23] A. Lehnert, S. Rusponi, M. Etzkorn, S. Ouazi, P. Thakur, and H. Brune, Phys. Rev. B **81**, 104430 (2010).
[24] E. Stavitski and F. M. F. de Groot, Micron **41**, 687 (2010).
[25] See Supplemental Material at http://link.aps.org/supplemental/10.1103/PhysRevLett.113.177201, which includes Refs. [26–51], for details about STM experiments, multiplet calculations, XAS and XMCD data analysis, as well as for further XAS and XMCD measurements on Co single adatoms on Ru(0001) and Ir(111) and small Co clusters on graphene.
[26] R. Gaisch, J. K. Gimzewski, B. Reihl, R. R. Schlittler, M. Tschudy, and W.-D. Schneider, Ultramicroscopy **42–44**, 1621 (1992).
[27] E. Loginova, N. C. Bartelt, P. J. Feibelman, and K. F. McCarty, New J. Phys. **11**, 063046 (2009).
[28] P. W. Sutter, J.-I. Flege, and E. A. Sutter, Nat. Mater. **7**, 406 (2008).
[29] H. Brune, Surf. Sci. Rep. **31**, 125 (1998).
[30] P. Błoński, A. Lehnert, S. Dennler, S. Rusponi, M. Etzkorn, G. Moulas, P. Bencok, P. Gambardella, H. Brune, and J. Hafner, Phys. Rev. B **81**, 104426 (2010).
[31] H. Brune, *Physics of Covered Solid Surfaces*, edited by H. P. Bonzel, Landolt Börnstein New Series, Group III: Condensed Matter Vol. III/42, subvolume A, Part 1 (Springer, Berlin, 2001), p. 217.
[32] M. Gyamfi, T. Eelbo, M. Wasniowska, and R. Wiesendanger, Phys. Rev. B **84**, 113403 (2011).
[33] V. Madhavan, W. Chen, T. Jamneala, M. F. Crommie, and N. S. Wingreen, Science **280**, 567 (1998).
[34] A. F. Otte, M. Ternes, K. v. Bergmann, S. Loth, H. Brune, C. P. Lutz, C. F. Hirjibehedin, and A. J. Heinrich, Nat. Phys. **4**, 847 (2008).
[35] G. E. Pacchioni, M. Pivetta, L. Gragnaniello, F. Donati, S. Rusponi, and H. Brune (unpublished).
[36] A. Abragam and B. Bleaney, *Electron Paramagnetic Resonance of Transition Ions* (Clarendon, Oxford, 1970).
[37] J. C. Hempel and M. E. Miller, J. Chem. Phys. **75**, 2959 (1981).
[38] J. Stöhr and D. A. Outka, Phys. Rev. B **36**, 7891 (1987).
[39] C. Brouder, J. Phys. Condens. Matter **2**, 701 (1990).
[40] H. Brune and P. Gambardella, Surf. Sci. **603**, 1812 (2009).
[41] C. Etz, J. Zabloudil, P. Weinberger, and E. Y. Vedmedenko, Phys. Rev. B **77**, 184425 (2008).
[42] D. Martoccia, P. R. Willmott, T. Brugger, M. Björck, S. Günther, C. M. Schlepütz, A. Cervellino, S. A. Pauli, B. D. Patterson, S. Marchini, J. Wintterlin, W. Moritz, and T. Greber, Phys. Rev. Lett. **101**, 126102 (2008).
[43] W. Moritz, B. Wang, M.-L. Bocquet, T. Brugger, T. Greber, J. Wintterlin, and S. Günther, Phys. Rev. Lett. **104**, 136102 (2010).
[44] Q. Dubout, F. Calleja, G. Sclauzero, M. Etzkorn, A. Lehnert, L. Claude, M. Papagno, F. D. Natterer, F. Patthey, S. Rusponi, A. Pasquarello, and H. Brune (unpublished).

[45] F. D. Natterer, F. Patthey, and H. Brune, Phys. Rev. Lett. **109**, 066101 (2012).
[46] F. D. Natterer, F. Patthey, and H. Brune, Surf. Sci. **615**, 80 (2013).
[47] F. Donati, Q. Dubout, G. Autès, F. Patthey, F. Calleja, P. Gambardella, O. V. Yazyev, and H. Brune, Phys. Rev. Lett. **111**, 236801 (2013).
[48] The valleys of the moiré correspond to the regions with the C-Ru stacking $(C, C) = (\text{top}, \text{fcc})$ and $(C, C) = (\text{hcp}, \text{top})$, while the hills correspond to the $(C, C) = (\text{fcc}, \text{hcp})$.
[49] J. Ren, H. Guo, J. Pan, Y. Y. Zhang, X. Wu, H.-G. Luo, S. Du, S. T. Pantelides, and H.-J. Gao, Nano Lett. **14**, 4011 (2014).
[50] T. Eelbo, M. Waśniowska, P. Thakur, M. Gyamfi, B. Sachs, T. O. Wehling, S. Forti, U. Starke, C. Tieg, A. I. Lichtenstein, and R. Wiesendanger, Phys. Rev. Lett. **110**, 136804 (2013).
[51] B. T. Thole, P. Carra, F. Sette, and G. van der Laan, Phys. Rev. Lett. **68**, 1943 (1992).
[52] P. Carra, B. T. Thole, M. Altarelli, and X. Wang, Phys. Rev. Lett. **70**, 694 (1993).
[53] S. Stepanow, A. Mugarza, G. Ceballos, P. Moras, J. C. Cezar, C. Carbone, and P. Gambardella, Phys. Rev. B **82**, 014405 (2010).
[54] P. Gambardella, S. S. Dhesi, S. Gardonio, C. Grazioli, P. Ohresser, and C. Carbone, Phys. Rev. Lett. **88**, 047202 (2002).
[55] P. Gambardella, S. Rusponi, M. Veronese, S. S. Dhesi, C. Grazioli, A. Dallmeyer, I. Cabria, R. Zeller, P. H. Dederichs, K. Kern, C. Carbone, and H. Brune, Science **300**, 1130 (2003).
[56] T. Eelbo, M. Waśniowska, M. Sikora, M. Dobrzański, A. Kozłowski, A. Pulkin, G. Autès, I. Miotkowski, O. V. Yazyev, and R. Wiesendanger, Phys. Rev. B **89**, 104424 (2014).
[57] Multiplet calculations reveal a dipolar term $m_D = 0.45\ \mu_B$, parallel to m_S at normal incidence. Including it, we obtain $m_L(0°)/m_S(0°) = 0.86$, which emphasizes, even more, the large anisotropy of m_L.
[58] M. Höck and J. Schnack, Phys. Rev. B **87**, 184408 (2013).
[59] H. Ebert, J. Stöhr, S. S. P. Parkin, M. Samant, and A. Nilsson, Phys. Rev. B **53**, 16067 (1996).
[60] Using Eq. (1) with $m = 2\ \mu_B$ and $K < 0$, one observes that $M = 0.9 M_{\text{sat}}$ at $B = 6.8$ T can be reached only for $T \leq 1$ K along the grazing incidence direction.
[61] A. B. Preobrajenski, M. L. Ng, A. S. Vinogradov, and N. Mårtensson, Phys. Rev. B **78**, 073401 (2008).
[62] T. Brugger, S. Günther, B. Wang, H. Dil, M.-L. Bocquet, J. Osterwalder, J. Wintterlin, and T. Greber, Phys. Rev. B **79**, 045407 (2009).
[63] D. Stradi, S. Barja, C. Díaz, M. Garnica, B. Borca, J. J. Hinarejos, D. Sánchez-Portal, M. Alcamí, A. Arnau, A. L. Vázquez de Parga, R. Miranda, and F. Martín, Phys. Rev. B **88**, 245401 (2013).
[64] P. Sutter, J. T. Sadowski, and E. Sutter, Phys. Rev. B **80**, 245411 (2009).
[65] I. Pletikosić, M. Kralj, P. Pervan, R. Brako, J. Coraux, A. T. NDiaye, C. Busse, and T. Michely, Phys. Rev. Lett. **102**, 056808 (2009).
[66] S. Rusponi, M. Papagno, P. Moras, S. Vlaic, M. Etzkorn, P. M. Sheverdyaeva, D. Pacilé, H. Brune, and C. Carbone, Phys. Rev. Lett. **105**, 246803 (2010).
[67] J. Stöhr and H. C. Siegmann, *Magnetism—From Fundamental to Nanoscale Dynamics* (Springer, Berlin, 2006).
[68] I. G. Rau, S. Baumann, S. Rusponi, F. Donati, S. Stepanow, L. Gragnaniello, J. Dreiser, C. Piamonteze, F. Nolting, S. Gangopadhyay, O. R. Albertini, R. M. Macfarlane, C. P. Lutz, B. A. Jones, P. Gambardella, A. J. Heinrich, and H. Brune, Science **344**, 988 (2014).

Supplementary Material for "Tailoring the magnetism of Co atoms on graphene through substrate hybridization"

F. Donati,[1] L. Gragnaniello,[1] A. Cavallin,[1] F. D. Natterer,[1] Q. Dubout,[1]
M. Pivetta,[1] F. Patthey,[1] J. Dreiser,[2,1] C. Piamonteze,[2] S. Rusponi,[1] and H. Brune[1]

[1] *Institute of Condensed Matter Physics (ICMP), Ecole Polytechnique Fédérale de Lausanne (EPFL), Station 3, CH-1015, Switzerland*
[2] *Swiss Light Source (SLS), Paul Scherrer Institut (PSI), CH-5232 Villigen PSI, Switzerland*

I. EXPERIMENTAL SETUP FOR LOW TEMPERATURE STM MEASUREMENTS

The low-temperature STM measurements were performed with a homemade STM, operating at 4.7 K and in an ultra-high vacuum (UHV) chamber with a base pressure of $p < 5 \times 10^{-11}$ mbar [1]. Sample preparation and characterization were carried out in the same UHV system. We cleaned the surfaces of the Ru(0001) and Ir(111) single crystals by repeated cycles of Ar^+ sputtering (10 μA/cm^2, 1 kV, 300 K, 30 min) and flash to 1500 K. Surface cleanliness was checked with STM and the stated preparation procedure repeated, if deemed necessary after STM inspection. On Ru, graphene (G) was either grown by chemical vapor deposition (CVD) [2, 3] at 1000 K, using an ethylene partial pressure of 1×10^{-6} mbar for 10 min, or by simply heating to 1200 K the Ru crystal that has been loaded in deeper layers by C atoms through several CVD cycles before [3, 4]. On Ir, graphene was grown by CVD at 1300 K using an ethylene partial pressure of 1×10^{-7} mbar for 3 min. Subsequent to graphene growth, the samples were transferred at room temperature to the STM and cooled to 10 K. Cobalt atoms were dosed from a high purity rod with an e-beam evaporator and the sample in the STM position and at $T = 10$ K. We carried out several preliminary deposition cycles onto the cooled and closed radiation shield of the cryostat in order to achieve a background pressure in the 10^{-11} mbar range during the actual deposition [5]. This procedure suppresses the detrimental hydrogen co-adsorption [5, 6]. The Co atom flux was calibrated at low coverages with the STM at $T = 4.7$ K by measuring the density of monomers on atomically clean Ru and Ir terraces. Coverages (Θ) are given in monolayers (ML), where one ML is defined as one Co atom per substrate atom. Scanning tunneling spectroscopy was performed by recording the bias-dependent differential conductance (dI/dV) using a lock-in amplifier and adding a sinusoidal 2 mV peak-to-peak modulation at 397 Hz to the bias voltage. We used platinum-iridium tips for all measurements and the constant current mode for topographic STM images.

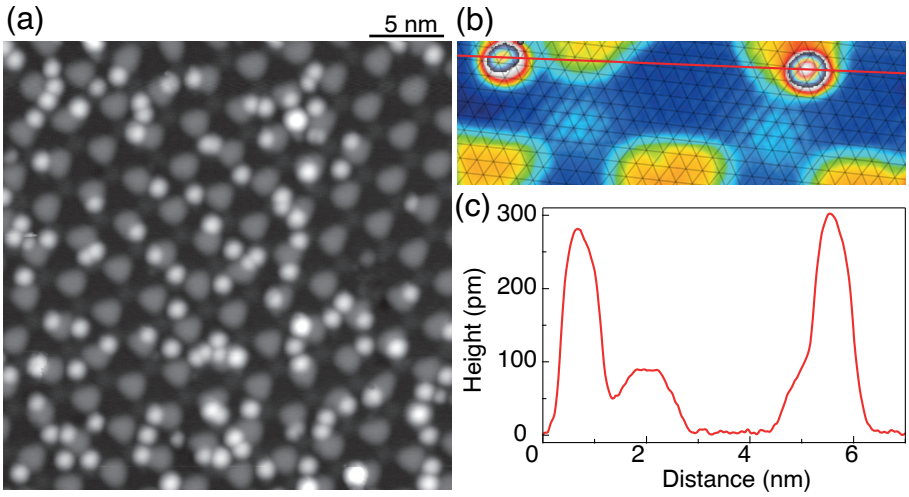

Figure S1. STM images of Co/G/Ru(0001)–(23 × 23). (a) Macroscopic view of the Co adatom distribution ($\Theta = 0.074$ ML, $V_t = -50$ mV, $I_t = 100$ pA, $T = 4.7$ K). (b) Zoom into two Co adatoms with atomically resolved graphene ($V_t = -20$ mV, $I_t = 500$ pA). The superimposed lattice marks graphene hollow sites. The left-handed atom is a representative of the major population, whereas the right atom shows a minority Kondo atom, see Fig. S2. (c) Apparent height profile across the red line shown in (b).

II. COBALT DEPOSITION AND ADATOM CHARACTERIZATION

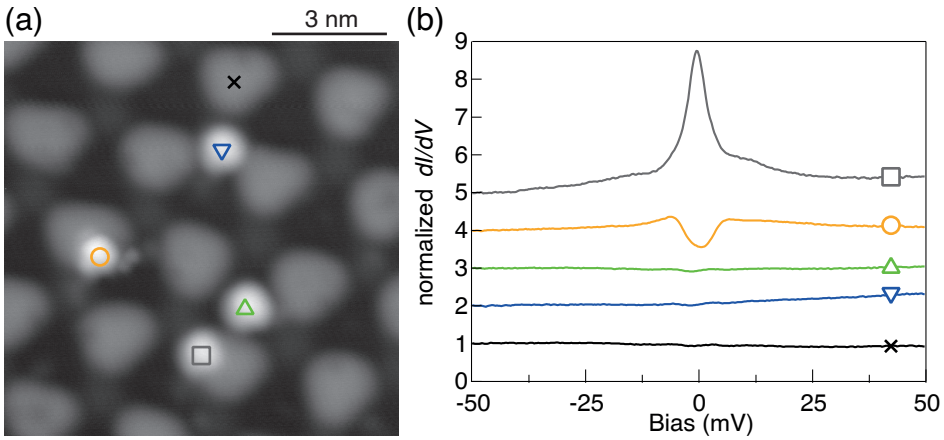

Figure S2. (a) STM image of Co atoms on G/Ru(0001) that are used to exemplify their differential conductance characteristics depending on the moiré stacking region onto which they are adsorbed ($\Theta = 0.074$ ML, $V_t = -50$ mV, $I_t = 200$ pA, $T = 4.7$ K). The majority, 81 ± 2 %, of the Co adatoms are featureless in their respective dI/dV spectra and are found in the (C,C)=(top, fcc) [Δ] and (C,C)=(hcp, top) [∇] stacking regions, whereas Co adatoms on the moiré hills show either dips [$\square$] or peaks [$\bigcirc$] in dI/dV ($R_g = 2.5 \times 10^8$ Ω). These are the Kondo screened adatoms which do not contribute to the XMCD signal.

Figure S1 shows the G/Ru(0001)–(23×23) superstructure [7] after dosing $(7.4 \pm 0.2) \times 10^{-3}$ ML Co at $T = 10$ K. To precisely determine the mean Co cluster size, as well as to assess the adatom mobility, we adopted two different approaches. In the first, Co was deposited onto samples with a partial G coverage. Since both coexisting surface terminations are exposed to the same adatom flux, the ratio of the mean Co cluster sizes on the two terminations can be precisely determined from the areal density ratio of Co clusters. Assuming a cluster size of 1.02 for Co on Ru, as expected from statistical growth for such a low Co coverage on a metal surface [8, 9], the ratio yields 1.01 $\pm$ 0.04 atoms per Co cluster on graphene, *i.e.*, the clusters are essentially monomers. In the second, we performed a statistical analysis of the apparent height of the Co clusters on G/Ru(0001) using the the bottom of the moiré pattern as the reference. We observed two classes of apparent heights. 93.0 ± 0.4 % of the species are imaged with a height of $2.8 - 3.0$ Å, depending on where they are adsorbed in the moiré unit cell, while 7.0 ± 0.4 % are imaged with a height of 3.6 ± 0.1 Å(at the same bias, the apparent moiré corrugation is 1.2 ± 0.05 Å). If we attribute the latter to dimers, the second approach yields 7 % dimers, 93 % monomers, and implies that the atoms make at least one jump after adsorption before they thermalize and become immobile [8]. We note that the minority species can also be adatoms that are on other adsorption sites. Consecutive STM images of the Co monomers prove their immobility on both surface terminations at temperatures below 5 K, which indicate that diffusion and aggregation could occur as regular thermal diffusion during the deposition at 10 K, by transient mobility that is absent on metal surfaces [10], or as an effect of the corrugated moiré pattern [11].

The preferred adsorption regions, where 81 ± 2 % of the Co adatoms are found, are the strongly bound (C,C)=(top, fcc) and (C,C)=(hcp, top) parts of the (23×23) superstructure. Figure S1 (b) shows the atomically resolved graphene lattice, two Co monomers, and the line profile across both adatoms (c). The left-handed adatom is an example of the majority population considered in the main text, whereas the right Co atom is from the Kondo screened minority species, see Fig. S2. The superimposed lattice in Fig. S1 (b) displays the 6-fold graphene hollow sites and illustrates the ambiguity in the assignment of the actual adsorption site. The apparent height maxima of the Co adatoms are not aligned with respect to the centers of the adatom circumference ellipsoids. The apparent non-symmetric shape of the adatoms varies as a function of the moiré region on which the adatom is adsorbed and prevents a clear identification of the adsorption site. This effect could be a consequence of the giant apparent strain in the G/Ru(0001) structure that seemingly modulates the graphene hollow–hollow separation [12].

We made a differential conductance survey of 370 Co adatoms, such as for the ones found in Fig. S1. The classification of the Co adsorbate population by the signature of the respective dI/dV is exemplified in Fig. S2. Therein, we illustrate the three distinct species that can be found among the Co adatoms. In agreement with the results of Ren *et al.* [13], for Co residing in the graphene (C,C)=(top, fcc) [Δ] and (C,C)=(hcp, top) [∇] regions, the dI/dV spectra are featureless within our experimental resolution. Conversely, Co adatoms on the edge of the moiré hills show Kondo resonances [14], *i.e.*, dips ($\bigcirc$) and peaks ($\square$) at the Fermi energy. Among the whole population, only 19 ± 2 % of the

Co atoms are Kondo screened. Note that no atoms were found to adsorb in the center of the moiré hills, in line with Ref. [13]. Convoluting a Fano function taking temperature and modulation broadening into account, we find a Kondo temperature of $T_K = 32 \pm 1$ K. The observed Kondo behaviour suggests a doublet ground state with $S_z = 1/2$, which can be observed in pure $S = 1/2$ systems or in systems with half-integer S and out-of-plane hard axis [15]. Note that these adatoms do not contribute to the XMCD signal [16], therefore the dichroism stems from the featureless Co adatoms adsorbed in the (C,C)=(top, fcc) and (C,C)=(hcp, top) regions. In particular, XMCD measurements reveal for this species a high spin ground state doublet with $S \approx 1.25$ (see main text). We therefore conclude that the spatially modulated graphene-substrate hybridization featured by the different moiré regions has a strong effect on the ground state of a Co atom, in line with the conclusions presented in the main text. Ren *et al.* observed that depositing Co with the sample kept at a higher temperature (20 K) results in a different population of the two species, with about 50 % of the Co atoms showing a Kondo peak [13]. We deduce that the higher temperature of the sample allows diffusion of the Co atoms towards the energetically most favorable edges of the moiré hills, as also observed for Fe atoms on G/Ru(0001) [11].

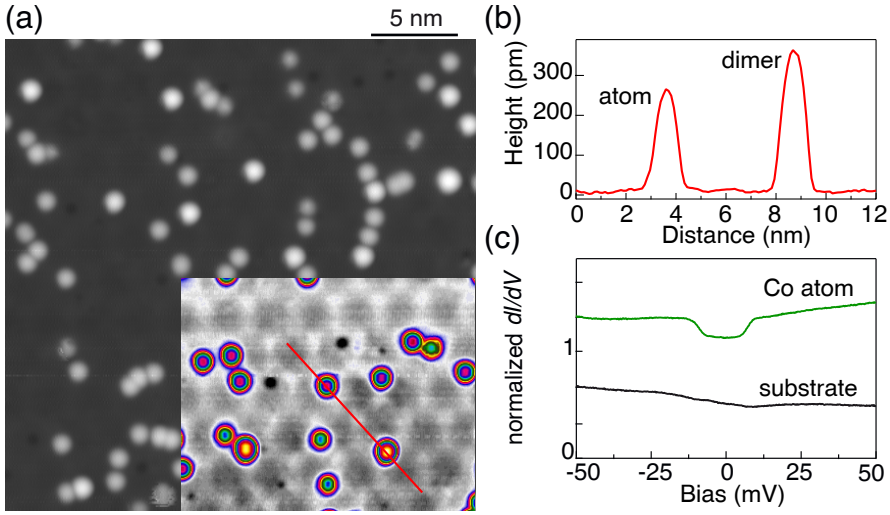

Figure S3. (a) STM image of Co atoms on G/Ir(111) ($\Theta = 0.007$ ML, $V_t = -100$ mV, $I_t = 70$ pA, $T = 4.7$ K). In the bottom right corner the contrast has been enhanced to emphasize the graphene moiré pattern. (b) Apparent height profile across the red line shown in (a). The majority (80 ± 5 %) of the objects are Co adatoms showing clear inelastic steps in dI/dV spectra (b) at 8.0 ± 0.5 mV (feedback loop stabilized at V_t = -0.1 V, I_t = 2 nA, V_{mod} = 1 mV). The minority (20 ± 5 %), are larger objects with apparent height of 380 ± 10 pm and identified as dimers.

An STM image of $(7 \pm 1) \times 10^{-3}$ ML of Co on G/Ir(111) deposited at $T = 10$ K is shown in Fig. S3 (a). Again, there are two classes of apparent cluster heights; 80 ± 5 % are imaged 2.7 ± 0.1 Å high while this time a larger fraction of 20 ± 5 % are imaged 3.8 ± 0.1 Å high, see Fig. S3 (b). Contrary to G/Ru(0001), the corrugation of the moiré pattern of G/Ir(111), (10 pm), is here negligible in comparison to the apparent height of a Co atom. Similarly to Co/G/Ru(0001), the relative amount of dimers is larger than the one expected from a purely statistical growth [8]. Since both monomers and dimers are immobile at $T = 4.7$ K, we again infer that the monomers diffuse a few atomic distances, either by transient or by thermal mobility, during the deposition at 10 K. The dI/dV spectrum of a Co atom does not depend on the position within the moiré cell. As shown in Fig. S3 (b), we observe two conductance steps at $|V_t| = 8.0 \pm 0.5$ mV. A very similar spectrum was observed for Co/G/Pt(111) [6], for which the conductance steps were proven to have magnetic origin. Moreover, as observed from XMCD measurements and inferred from multiplet calculations, for Co/G/Ir we find an out-of-plane hard axis, a number of holes in the d-orbitals of $n_h = 1.85$ and thus a corresponding $S \approx 1$, also in great similarity to Co/G/Pt. The absence of a Kondo resonance in the dI/dV spectrum of Co/G/Ir allows us to exclude a half-integer spin as the ground state [15], and provides further support to the conclusion of a $S \approx 1$ system. Therefore the conductance steps at ± 8 meV are very likely $m = 0 \rightarrow \pm 1$ excitations as reported for Co/G/Pt(111) [6].

III. MULTIPLET CALCULATIONS OF XAS AND XMCD SPECTRA

Simulated XAS and XMCD spectra were calculated using the CTM4XAS55 code [17]. It is based on an atomic multiplet model which takes into account electron-electron interaction, charge transfer to the ligand through configuration interaction, crystal field potential and spin-orbit coupling. Rescaled Slater-Condon integrals account for p and d electron-electron interaction. Charge transfer to the ligand is enabled via hopping terms reflecting the symmetry of the atomic environment. With the aim of reproducing the adsorption on top and hollow graphene site, two different atomic environments were considered. Since the uniaxial term is expected to dominate over the transverse terms, we model the crystal field potential in a $C_{\infty v}$ symmetry. In such an environment, the Co 3d-orbitals split into the a_1 singlet (d_{z^2}) and the two doublets e_1 (d_{xz}, d_{yz}) and e_2 ($d_{x^2-y^2}, d_{xy}$), respectively [18]. For the hollow site, this is fully justified since the 6^{th}-order transverse term stemming from the C_{6v} symmetry has no effect on the d-orbitals, therefore the crystal field is expected to be perfectly uniaxial [19]. For the three-fold symmetric top sites, the Co atom is directly bound to the underneath C atom, which provides the uniaxial field. The three adjacent C atoms weakly interact with the Co d-orbitals, therefore the C_{3v} transverse term is expected to be small. Moreover, this term only mixes orbitals belonging to different symmetries, without lifting the two-fold degeneracy of the e_1 and e_2 doublets [19]. Thus, it is expected to have small effect on the total spin and orbital moments and it is hence neglected.

Although the two adsorption sites were modeled with the same uniaxial symmetry, the splitting of the 3d-orbitals is expected to be different as a consequence of the local interaction with the ligand. Predictions for Co adsorbing on the top-site indicated that the a_1 orbital hybridizes with the C π orbital underneath, while the e_1 and e_2 are only slightly perturbed. Consequently, the a_1 singlet is lower in energy with respect to the two e doublets, which are almost degenerate [20]. For the hollow-site adsorption, the Co e_2 orbitals were predicted to hybridize with the π orbitals of the honeycomb C ring and are lowest in energy [20, 21]. The a_1 singlet is instead almost unperturbed by the ligand and it lies slightly higher in energy. Symmetry restrictions prevent e_1 orbitals to hybridize with π, therefore the repulsion with the honeycomb ring charge lifts up the energy of this doublet [6, 20, 21].

The energy splitting calculated with DFT was used as initial guess for the crystal field parameters. Together with the other model parameters, they were varied in a trial-and-error procedure until both the XAS and XMCD were correctly reproduced. The obtained energy splitting, as well as the 3d orbital occupancies, are the results of this optimization procedure and therefore reflect the overall influence of the graphene and its hybridization with the substrate on the Co atoms. For Co/G/Ru(0001), XAS and XMCD spectra were best reproduced using a mixed d^7 + d^8L configuration, with a 3d-splitting corresponding to the top-site adsorption, see Fig. 2(c). Model parameters have been varied until both normal incidence XAS and XMCD were correctly simulated. We found values for the uniaxial crystal field terms $Ds = 0.4$ eV and $Dt = 0.23$ eV. Configuration interaction is allowed respecting the $C_{\infty \text{v}}$ symmetry, therefore we used the hopping integrals $t(a_1) = 0.8$ eV, $t(e_1) = 0.5$ eV and $t(e_2) = 0.25$ eV. The charge transfer energy Δ and the core-hole interaction $U_{p-d} - U_{d-d}$ were set to -1.8 eV and 1.1 eV, respectively. The Slater-Condon integrals have been rescaled to 72 % to account for the chemical bonding. Valence band spin-orbit coupling was re-scaled to 99 %. Transition amplitudes for L_2 and L_3 were calculated in a dipolar approximation and broadened with Lorentzian functions of FWHM = 0.4 and 0.15 eV, respectively, to reproduce the experimental spectra. Further gaussian broadening of 0.15 eV is introduced to account for the finite experimental energy resolution.

For Co/G/Ir(111), agreement with experimental spectra was obtained assuming a mixed d^8 + d^9L configuration with the Co atom adsorbed at the hollow-site, see Fig. 4(c). We set the values of the uniaxial crystal field terms to $Ds = -0.17$ eV and $Dt = 0.12$ eV, and the hopping integrals $t(a_1) = 0.0$ eV, $t(e_1) = t(e_2) = 0.6$ eV. The charge transfer energy Δ and the core-hole interaction $U_{p-d} - U_{d-d}$ were set to 0.1 eV and 0.7 eV, respectively. The Slater-Condon integrals have been rescaled to 56 % to account for the larger overlap between the Co and ligand wavefunctions. Core and valence band spin-orbit coupling were re-scaled to 104 and 98 %, respectively. The stronger hybridization between Co and graphene is responsible for a larger Lorentzian broadening of the L_2 and L_3 edges of 0.6 and 0.3 eV, respectively. To increase the signal-to-noise ratio, Co/G/Ir(111) spectra were acquired with a higher flux but lower energy resolution, which is being accounted for by a larger gaussian broadening of 0.3 eV.

IV. ANGULAR DEPENDENCE OF THE INTEGRATED XAS AND CORRECTION TO THE SUM RULES

Quantitative values of the orbital moment (m_{L}) and the effective spin moment ($m_{\text{S+D}}$) projected on to the X-ray incidence direction can be obtained from the sum rules [22, 23]:

$$m_{\text{L}} = -\frac{2q}{t^{\text{ISO}}} n_{\text{h}}, \tag{S1}$$

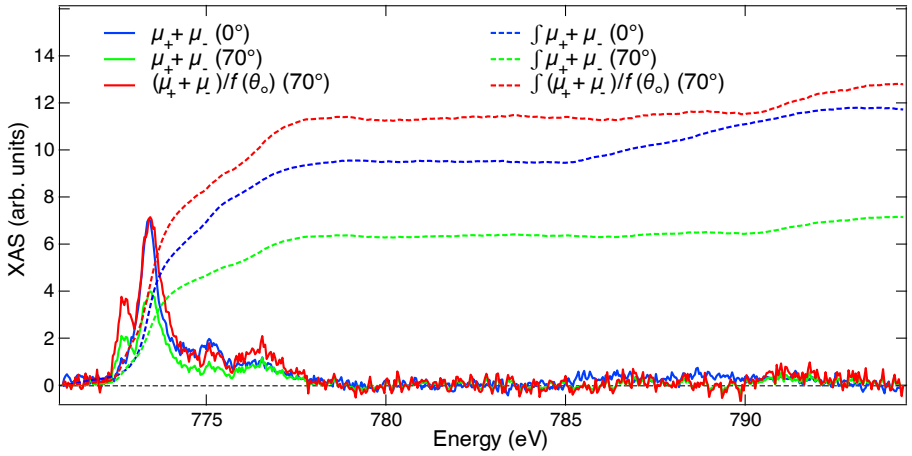

Figure S4. XAS spectra of Co atoms on G/Ru(0001) taken at normal and grazing incidence (Θ = 0.01 ML, B = 6.8 T, T = 2.5 K). Normal and grazing incidence curves were averaged over 10 and 5 spectra, respectively and normalized to their values at 768.5 eV.

$$m_{\mathrm{S+D}} = -\frac{9p - 6q}{t^{\mathrm{ISO}}} n_{\mathrm{h}}, \tag{S2}$$

where $p = \int_{L_3}(\mu_+ - \mu_-)dE$, $q = \int_{L_3+L_2}(\mu_+ - \mu_-)dE$, and $t^{\mathrm{ISO}} = \int_{L_3+L_2}(\mu_+ + \mu_- + \mu_0)dE$.

Here, $m_{\mathrm{S+D}}$ is the sum of the spin and the dipole spin moments. In principle, the evaluation of the isotropic term t^{ISO} requires the knowledge of the linear absorption intensity μ_0, to be measured with the linear polarization parallel to the magnetization direction and to the surface normal. This alignment is practically difficult to achieve and μ_0 is therefore often approximated by the mean $(\mu_+ + \mu_-)/2$. Although this approximation is generally valid for metals, particular care has to be adopted for highly anisotropic systems [24–26]. As shown in Fig. 2 of the manuscript, the integrated XAS $\mu_+ + \mu_-$ strongly depends on the angle of incidence, therefore its integral cannot be taken as a good approximation of t^{ISO}. Nevertheless, an estimation of this term can be obtained from the angular dependence of the absorption intensity $f(\theta_0)$, where θ_0 is the incidence angle of the photon beam with respect to the surface normal [26]. In a single-electron picture, the angular dependence of the integrated XAS for excitation to $d_{\mathrm{x^2-y^2}}$ and d_{xy} orbitals follows $f(\theta_0) = (1 + \cos^2\theta_0)/2$. Fig. S4 shows the comparison between the integrated XAS at the L_3 edge for normal and grazing incidence, together with the grazing incidence spectrum divided by $f(70°)$. The most intense excitation at 773.2 eV perfectly scales with $f(70°)$, which indicates an almost pure transition to the planar d orbitals. Although the other XAS features do not follow the same angular variation, we note that the integral of the XAS over the $L_{2,3}$ edges for grazing incidence rescaled by $f(70°)$ approaches the corresponding value at normal incidence. Therefore, we infer that the XAS spectrum is, to a very good extent, dominated by a single-electron-like excitation to the planar d orbitals, and that the integral t^{ISO} at different angles can be safely approximated with the function $3t(\theta_0)/2f(\theta_0)$, where $t(\theta_0) = \int_{L_3+L_2} \mu_+(\theta_0) + \mu_-(\theta_0)$.

V. SIMULATED MAGNETIZATION CURVES FROM A SPIN HAMILTONIAN

In addition to the model presented in the main text, magnetization curves acquired for Co atoms on G/Ru(0001) have further been modeled using a quantum mechanical approach. We described the spin states of a Co atom using the following spin hamiltonian:

$$\hat{H}_{spin} = g\mu_{\mathrm{B}}\hat{\mathbf{S}} \cdot \mathbf{B} + D\hat{S}_z^2\,, \tag{S3}$$

where g is the electron Landé factor, $\mathbf{B}$ denotes the external magnetic field, D the uniaxial anisotropy parameter, and $\hat{S}$ the effective spin operator. The z-axis was chosen by convention such as to maximize $|D|$. We modeled our system with an effective spin $S = 3/2$, therefore assuming half-integer ground and first excited state doublets. The expectation values of the magnetization along the beam axis as a function of external field $\mathbf{B}$ were obtained by:

$$\langle M_{\theta_0}\rangle = g\langle S_{\theta_0}\rangle = g\frac{\sum_{\mathrm{i}=1}^{2S+1}\langle\phi_{\mathrm{i}}|S_{\theta_0}|\phi_{\mathrm{i}}\rangle \exp\left(\epsilon_{\mathrm{i}}/k_{\mathrm{B}}T\right)}{\sum_{\mathrm{i}=1}^{2S+1}\exp\left(\epsilon_{\mathrm{i}}/k_{\mathrm{B}}T\right)}\,. \tag{S4}$$

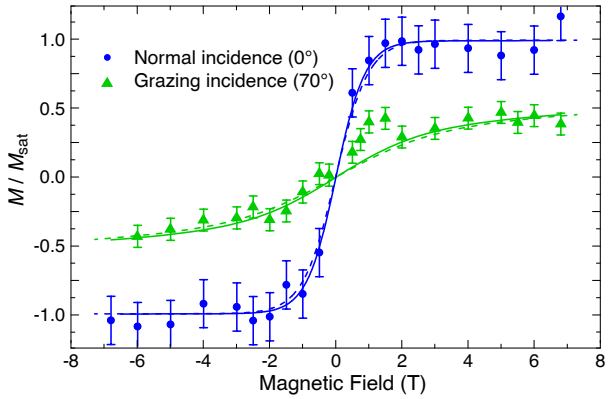

Figure S5. Magnetization curve of Co/G/Ru(0001) ($\Theta = 0.01$ ML, $T = 2.5$ K). The points are the maximum of the XMCD obtained from a single pair of μ_+ and μ_- spectra. Since each of them is measured on a different surface spot, we accounted for intensity variations by dividing by the maximum of the background subtracted XAS at the Co L_3 edge. The two curves were rescaled with respect to each other according to their effective total moment at $B = 6.8$ T, see Table 1 in the main text. Full lines: fits from Eq. (1) of the main text. Dashed lines: fits from the model described through Eq. (S4).

Here, $S_{\theta_0} = \sin\theta_0 S_x + \sin\theta_0 S_y + \cos\theta_0 S_z$ is the spin operator for an arbitrary incidence angle θ_0, ϕ_i and ϵ_i are the eigenstates and the eigenvalues obtained after diagonalizing the spin hamiltonian (S3). The model parameters g and D were adjusted to fit the experimental data. Both experimental and calculated magnetization curves are shown in Fig. S5. Little differences can be noticed between the semiclassical model (Eq. (1) from the main text) and the quantum mechanical model described through Eq. (S4). From the fit, we obtained $g = 2.55 \pm 0.6$ and $D = -3.6 \pm 1.5$ meV. Deviations from the free-electron g factor of 2 can be rationalized in term of mixed spin configurations and orbital contributions to the total magnetic moment, which can be significant for single adatoms [27]. For the assumed spin $S = 3/2$, we obtain a total magnetic moment $m_{tot} = g\mu_B S = 3.8 \pm 0.9\,\mu_B$ and a magnetic anisotropy $K = -D(S_z^2 - (1/2)^2) = -D((3/2)^2 - (1/2)^2) = -2D = 7.2 \pm 3$ meV, somewhat lower but in agreement within the error bars with the values found using Eq. (1) from the main text.

VI. MAGNETIC PROPERTIES OF SINGLE CO ATOMS ON RU(0001) AND ON IR(111)

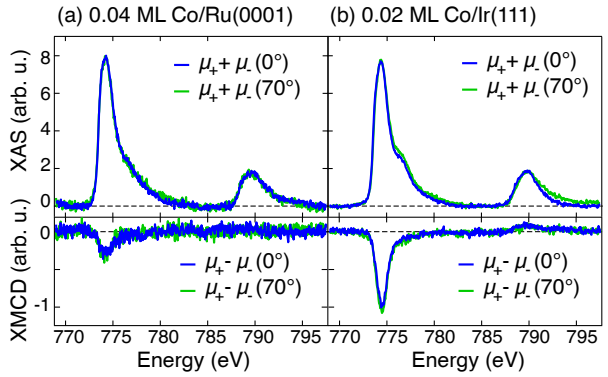

Figure S6. Normal and grazing incidence XAS and XMCD of (a) 0.04 ML Co/Ru(0001) and (b) 0.02 ML Co/Ir(111) ($T = 2.5$ K, $B = 6.8$ T).

In order to further evaluate the effect of the graphene layer on the magnetic properties of Co atoms, we performed XAS and XMCD measurements of single Co atoms on bare Ru(0001) and Ir(111) surfaces, see Fig. S6. As the adatom diffusion on metal surfaces is suppressed at the deposition temperature, the growth is statistical and a large majority of single atoms is expected up to 0.04 ML [8]. In contrast to Co/G/Ru(0001) (Fig. 2 of the main text), the XAS of Co/Ru(0001) (Fig. S6(a)) is devoid of any sharp multiplet structure, indicating a strong hybridization with the substrate. Moreover, the XMCD is almost quenched, which could be due to a ground state singlet $S \approx 0$

Table I. Effective spin and orbital magnetic moments per hole number (n_h), as well as their sum and ratio, of Co/Ru(0001) and Co/Ir(111) for normal and grazing incidence obtained from experiment using the sum rules. For Co/Ru(111), the ratio is not indicated because the errors are larger than the corresponding values.

	Co/Ru(0001) (0°)	Co/Ru(0001) (70°)	Co/Ir(111) (0°)	Co/Ir(111) (70°)
m_{S+D} (μ_B/n_h)	0.03 ± 0.02	0.04 ± 0.02	0.19 ± 0.04	0.18 ± 0.03
m_L (μ_B/n_h)	0.06 ± 0.05	0.06 ± 0.03	0.07 ± 0.02	0.08 ± 0.02
$m_{S+D} + m_L$ (μ_B/n_h)	0.09 ± 0.03	0.10 ± 0.04	0.26 ± 0.04	0.26 ± 0.04
m_L/m_{S+D}	–	–	0.37 ± 0.17	0.44 ± 0.18

or to a Kondo-screened $S \approx 1/2$. The widths of the $L_{2,3}$ edges in the XAS of Co/Ir(111) (Fig. S6(b)) also suggest a relatively strong Co-substrate hybridization. The XMCD is identical for the two sample orientations, indicating negligible anisotropy. Table I summarizes the magnetic moments per hole number obtained from the sum rules. For Co/Ru(0001), the moments are reduced by an order of magnitude and only a negligible anisotropy is seen, in strong contrast with the results observed on Co/G/Ru. For Co/Ir(111), the magnetic moments are somehow comparable to the corresponding ones measured for Co/G/Ir(111). In this case, the role of graphene is evident from the different anisotropy, which is almost absent for Co on the bare surface while it favors in-plane magnetization in the presence of graphene. The very low anisotropy found for Co/Ir(111) is in qualitative agreement with former predictions [28], where it was calculated to be 3 times smaller than the one of Co/Pt(111).

VII. MAGNETIC PROPERTIES OF SMALL CO CLUSTERS ON G/RU(0001) AND ON G/IR(111)

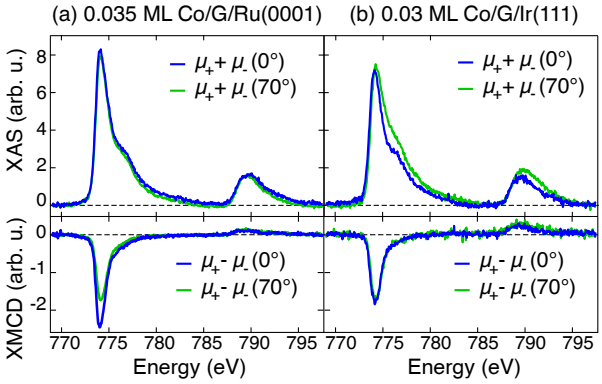

Figure S7. Normal and grazing incidence XAS and XMCD of (a) 0.035 ML Co/G/Ru(0001) and (b) 0.03 ML Co/G/Ir(111) ($T = 2.5$ K, $B = 6.8$ T).

To disentangle the magnetic signal of the monomers from the ones of dimers and small clusters, we performed XAS and XMCD measurements increasing the Co coverage and, consequently, the relative amount of clusters in the ensemble [8]. The growth of small clusters on graphene can be initiated at a relatively lower coverage with respect to bare metal surfaces as a consequence of the smaller diffusion barrier and the corrugated moiré pattern [11]. As shown in Fig. 2, 4 and S7, the XAS and XMCD spectra for $\Theta = 0.01$ ML and $\Theta = 0.03$ ML are significantly different. In particular, the XAS of Co/G/Ru(0001) does not show any multiplet structure, indicating a strong hybridization of the Co orbitals and the formation of metallic bonds. In this case, a large majority of the Co atoms diffused to form dimers and small clusters. Similarly to the $\Theta = 0.01$ ML case, the dichroism is still larger at normal incidence, but its magnitude and anisotropy are significantly reduced. The corresponding values of the magnetic moments yielded by the sum rules are summarized in Table II. Also the anisotropy is strongly reduced in comparison to the monomer case. For Co/G/Ir(111), $\Theta = 0.03$ ML, the small differences between normal and grazing incidence XAS are reminiscent of the behavior observed for $\Theta = 0.01$ ML. However, the XMCD anisotropy is clearly different, see Table II for the quantitative analysis. The presence of small Co clusters in the ensemble clearly increases the normal component of the magnetization. We recall that about 20 % of the Co species were found to be small clusters at 0.01 ML. Extrapolating from our results observed for 0.01 ML to an ensemble of solely Co atoms on G/Ir(111), which would be realized for

Table II. Effective spin and orbital magnetic moments per hole number (n_h), as well as their sum, of small clusters of Co/G/Ru(0001) and Co/G/Ir(111) for normal and grazing incidence obtained from experiment using the sum rules.

	Co/G/Ru(0001) (0°)	Co/G/Ru(0001) (70°)	Co/G/Ir(111) (0°)	Co/G/Ir(111) (70°)
$m_{\mathrm{S+D}}$ ($\mu_\mathrm{B}/n_\mathrm{h}$)	0.38 ± 0.04	0.30 ± 0.03	0.36 ± 0.04	0.31 ± 0.03
m_L ($\mu_\mathrm{B}/n_\mathrm{h}$)	0.18 ± 0.02	0.13 ± 0.02	0.12 ± 0.02	0.07 ± 0.02
$m_{\mathrm{S+D}} + m_\mathrm{L}$ ($\mu_\mathrm{B}/n_\mathrm{h}$)	0.56 ± 0.05	0.43 ± 0.04	0.48 ± 0.05	0.38 ± 0.08
$m_\mathrm{L}/m_{\mathrm{S+D}}$	0.47 ± 0.10	0.43 ± 0.11	0.33 ± 0.09	0.23 ± 0.09

Co coverages well below the actual detection threshold of an XMCD experiment, one expects a lower normal XMCD signal than the one presented in Fig.4(a). We thereby consolidate our view of a significant magnetic anisotropy with in-plane easy axis for Co atoms on G/Ir(111).

[1] R. Gaisch, J. K. Gimzewski, B. Reihl, R. R. Schlittler, M. Tschudy, and W.-D. Schneider, Ultramicroscopy **42-44**, 1621 (1992).
[2] E. Loginova, N. C. Bartelt, P. J. Feibelman, and K. F. McCarty, New J. Phys. **11**, 063046 (2009).
[3] F. D. Natterer, S. Rusponi, M. Papagno, C. Carbone, and H. Brune, Journal of Physics: Condensed Matter **24**, 314203 (2012).
[4] P. W. Sutter, J.-I. Flege, and E. A. Sutter, Nat. Mater. **7**, 406 (2008).
[5] F. D. Natterer, F. Patthey, and H. Brune, Surf. Sci. **615**, 80 (2013).
[6] F. Donati, Q. Dubout, G. Autès, F. Patthey, F. Calleja, P. Gambardella, O. V. Yazyev, and H. Brune, Phys. Rev. Lett. **111**, 236801 (2013).
[7] D. Martoccia, P. R. Willmott, T. Brugger, M. Björck, S. Günther, C. M. Schlepütz, A. Cervellino, S. A. Pauli, B. D. Patterson, S. Marchini, J. Wintterlin, W. Moritz, and T. Greber, Phys. Rev. Lett. **101**, 126102 (2008).
[8] H. Brune, Surf. Sci. Rep. **31**, 121 (1998).
[9] P. Błoński, A. Lehnert, S. Dennler, S. Rusponi, M. Etzkorn, G. Moulas, P. Bencok, P. Gambardella, H. Brune, and J. Hafner, Phys. Rev. B **81**, 104426 (2010).
[10] H. Brune, *Physics of Covered Solid Surfaces*, edited by H. P. Bonzel, Landolt Börnstein New Series, Group III: Condensed Matter, Vol. III/42 Subvolume A, Part 1 (Springer, Berlin, 2001) p. 217.
[11] M. Gyamfi, T. Eelbo, M. Wasniowska, and R. Wiesendanger, Phys. Rev. B **84**, 113403 (2011).
[12] Q. Dubout, F. Calleja, G. Sclauzero, M. Etzkorn, A. Lehnert, L. Claude, M. Papagno, F. D. Natterer, F. Patthey, S. Rusponi, A. Pasquarello, and H. Brune, in preparation (2014).
[13] J. Ren, H. Guo, J. Pan, Y. Y. Zhang, X. Wu, H.-G. Luo, S. Du, S. T. Pantelides, and H.-J. Gao, Nano Lett. **14**, 4011 (2014).
[14] V. Madhavan, W. Chen, T. Jamneala, M. F. Crommie, and N. S. Wingreen, Science **280**, 567 (1998).
[15] A. F. Otte, M. Ternes, K. v. Bergmann, S. Loth, H. Brune, C. P. Lutz, C. F. Hirjibehedin, and A. J. Heinrich, Nat. Phys. **4**, 847 (2008).
[16] G. E. Pacchioni, M. Pivetta, L. Gragnaniello, F. Donati, S. Rusponi, and H. Brune, in preparation (2014).
[17] E. Stavitski and F. M. F. de Groot, Micron **41**, 687 (2010).
[18] A. Abragam and B. Bleaney, *Electron paramagnetic resonance of transition ions* (Clarendon Press, Oxford, 1970).
[19] J. C. Hempel and M. E. Miller, J. Chem. Phys. **75**, 2959 (1981).
[20] T. O. Wehling, A. V. Balatsky, M. I. Katsnelson, A. I. Lichtenstein, and A. Rosch, Phys. Rev. B **81**, 115427 (2010).
[21] A. N. Rudenko, F. J. Keil, M. I. Katsnelson, and A. I. Lichtenstein, Phys. Rev. B **86**, 075422 (2012).
[22] B. T. Thole, P. Carra, F. Sette, and G. van der Laan, Phys. Rev. Lett. **68**, 1943 (1992).
[23] P. Carra, B. T. Thole, M. Altarelli, and X. Wang, Phys. Rev. Lett. **70**, 694 (1993).
[24] J. Stöhr and D. A. Outka, Phys. Rev. B **36**, 7891 (1987).
[25] C. Brouder, J. Phys.: Condens. Matter **2**, 701 (1990).
[26] S. Stepanow, A. Mugarza, G. Ceballos, P. Moras, J. C. Cezar, C. Carbone, and P. Gambardella, Phys. Rev. B **82**, 014405 (2010).
[27] H. Brune and P. Gambardella, Surf. Sci. **603**, 1812 (2009).
[28] C. Etz, J. Zabloudil, P. Weinberger, and E. Y. Vedmedenko, Phys. Rev. B **77**, 184425 (2008).